Journal Pre-proof

3D Hierarchical Transition-Metal Sulfides Deposited on MXene as Binder-Free Electrode for High-Performance Supercapacitors

Hui Li, Xin Chen, Erfan Zalezhad, K.N. Hui, K.S. Hui, Min Jae Ko

Please cite this article as: Li H, Chen X, Zalezhad E, Hui KN, Hui KS, Ko MJ, 3D Hierarchical Transition-Metal Sulfides Deposited on MXene as Binder-Free Electrode for High-Performance Supercapacitors, *Journal of Industrial and Engineering Chemistry* (2019), doi: https://doi.org/10.1016/j.jiec.2019.10.028

3D Hierarchical Transition-Metal Sulfides Deposited on MXene as Binder-Free Electrode for High-Performance Supercapacitors

Hui Li[1,&], Xin Chen[2,&], Erfan Zalezhad[3,*], K. N. Hui[4,*], K. S. Hui[5,*] and Min Jae Ko[1,*]

[1]Department of Chemical Engineering, Hanyang University, 222 Wangsimni-ro, Seongdong-gu, Seoul, 04763, Republic of Korea

[2]Department of Mechanical Convergence Engineering, Hanyang University, 222 Wangsimni-ro, Seongdong-gu, Seoul, 04763, Republic of Korea

[3]Biomechacin LLC, San Antonio, TX 78251, USA

[4]Institute of Applied Physics and Materials Engineering, University of Macau, Avenida da Universidade, Taipa, Macau 999078, China

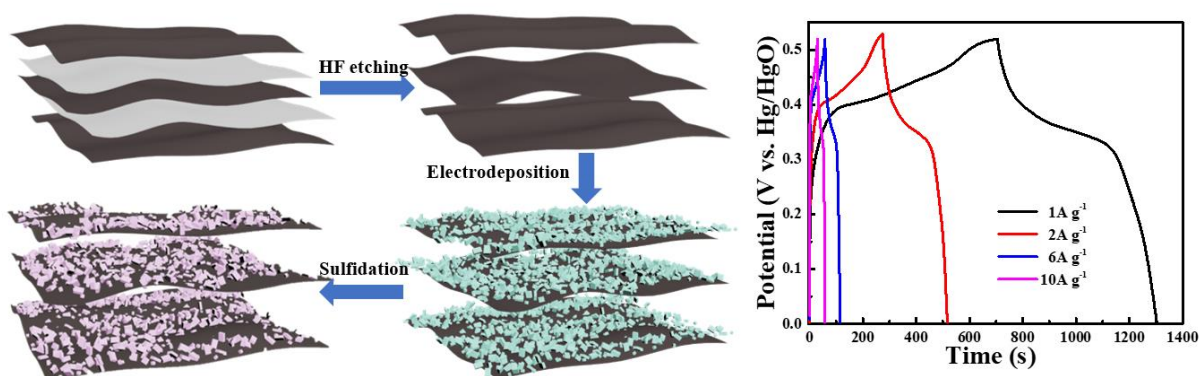[5]School of Mathematics, University of East Anglia, Norwich NR4 7TJ, UK

*Corresponding authors
E-mail: mjko@hanyang.ac.kr (M. J. Ko); e.zalnezhad@gmail.com (E. Zalnezhad); bizhui@umac.mo (K. N. Hui); k.hui@uea.ac.uk (K. S. Hui)

[&] These authors equally contributed to this work.

Graphical Abstract

Abstract

MXene has been considered as a promising two-dimensional material for supercapacitors owing to its large surface area, high conductivity, and excellent cycling stability. However, its low specific capacitance restricts its extensive applications. Therefore, to address the issue, we homogeneously deposited $NiCo_2S_4$ nanoflakes on the surface of MXene on conductive nickel foam (denoted as MXene-NiCo$_2$S$_4$@NF), which was used as a composite binder-free electrode for supercapacitor applications. The $NiCo_2S_4$ nanoflakes increased the surface area of the composite electrode, thereby increasing its specific capacity from 106.34 C g^{-1} to 596.69 C g^{-1} at 1 A g^{-1}. Compared to the pristine MXene, MXene-NiCo$_2$S$_4$@NF maintained the high retention rate of pristine MXene and exhibited excellent cycling stability with 80.4% of its initial specific capacity after 3000 cycles. The composite electrode exhibited improved electrochemical performance for supercapacitors, owing to the combined merits of $NiCo_2S_4$ (high specific capacity) and MXene (high retention rate and good cycling stability. The fabricated asymmetric solid-state supercapacitor using MXene-NiCo$_2$S$_4$ as a positive electrode and active carbon as a negative electrode, exhibited an energy density of 27.24 Wh kg^{-1} at 0.48

2

kW kg^{-1} of power density.

Keywords: MXene, NiCo$_2$S$_4$, binder-free, electrostatic interactions, asymmetric capacitor

Introduction

There have been extensive studies on innovative high-performance energy-storage devices owing to the increasing energy demand worldwide. Supercapacitors such as electrochemical capacitors (ECs) have a wide range of applications as complementary energy-storage devices to batteries in electric vehicles, wearable devices, and portable electronics owing to their fast charge–discharge performance, high power density, and excellent cycle life.*[1-7]* Based on their charge-storage mechanism, the ECs can be classified into two categories: 1) electrical double-layer capacitors (EDLCs), which are characterized by ion adsorption/desorption at the interlayer between the electrode and electrolyte, and 2) pseudocapacitors, which utilize a Faradaic redox reaction and provide higher capacitance. *There have been several reports on the active electrode materials, such as carbon materials, metal oxides, and conductive polymers.[8-15]*

MXenes were reported in 2011 as a novel family of two-dimensional graphene-like materials.[16] However, owing to their metallic conductivity and hydrophilicity, MXenes are better suited for the electrochemical applications compared with graphene, which is composed of a thin layer of carbon atoms. Furthermore, it is possible to modify the surface of the MXenes by selective chemical etching of their precursor without affecting their excellent electrical conductivity.[17, 18] The general chemical formula of Mxenes is $M_{n+1}X_nT_x$, where "M" is an early transition metal (e.g., Sc, Ti, V, or Cr), "X" is either carbon or nitrogen, "T" represents the functional groups on the surface (e.g., O-, OH-, or F-), and n = 1, 2, or 3. These can be synthesized by selectively etching off the A atom layer from the MAX phase, where "A" is

4

typically a Group 13 or 14 element.[19-22] In the field of capacitive energy storage, MXenes, which exhibit a large surface area, high conductivity, and excellent cycling stability, have been investigated as a novel electrode material for the ECs.[23, 24] Particularly, $Ti_3C_2T_x$-based ECs exhibit pseudocapacitive behavior in alkaline electrolytes, owing to their highly reversible surface redox reaction and metallic electrical conductivity.[25, 26] Furthermore, for the application of MXenes as a current collector, the powdery MXene materials must be mixed with conductive carbon or a polymeric binder, followed by pressing. However, the addition of such binders inevitably deteriorates the overall energy-storage capacity and electrical conductivity of the active materials. Therefore, a new concept of binder-free electrodes has been recently proposed[27, 28], wherein the clay-like $Ti_3C_2T_x$ materials are directly deposited on the nickel foam (NF) by a sample dropping-mild baking method without any binder, inducing good mechanical adhesion, higher surface area, and lower resistance. The adoption of a binder-free electrode could provide a high specific capacitance of 499 F g^{-1} and excellent cycling stability in acidic electrolytes. However, the specific capacitance of MXene-based binder-free electrodes is still unsatisfactory for further applications, owing to the relatively low amount of active sites of carbide materials.

To address this issue, many works have been reported on the composites of MXenes with transition-metal oxides (TMOs)[29, 30] or conductive polymers (CPs).[31-33] However, the low conductivity of the TMOs and CPs would result in poor rate capability and cycling stability in the charge-discharge process, respectively.[34-36] Moreover, most of the reported TMOs would be synthesized at high temperatures over 300 ℃; such high-temperature annealing causes the MXene to be partially oxidized, leading to conversion into TiO_2. Consequently, the

5

electrical conductivity of the MXenes would be significantly reduced, resulting in inferior rate capability.[37, 38] In contrast, transition-metal sulfides (TMSs) exhibit higher conductivity than the TMOs, owing to the stronger covalent nature of the former, which originates from the soft basic S^{2-}/S_2^{2-} ions, instead of the hard basic O^{2-} ions in the latter, which depend on the hard and soft acid and base theory.[39] Moreover, the hydrothermal sulfurization process below 130 ℃ effectively suppresses the oxidation of the MXenes. Furthermore, the binary TMSs are reported to retain better electrochemical activity and higher capacity than the mono-metal sulfides owing to their abundant redox sites.[9, 34] However, to the best of our knowledge, there have been no reports on a 3D hierarchical composite of MXene with $NiCo_2S_4$, the unique nanostructure provided larger surface area and exposed more redox sites of $NiCo_2S_4$ in electrolyte for application as energy-storage devices.

In this study, we fabricated $NiCo_2S_4$ on a $Ti_3C_2T_x$-based NF binder-free electrode (denoted as MXene-$NiCo_2S_4$@NF), which was then applied to the supercapacitors. The MXene-$NiCo_2S_4$@NF nanocomposite exhibited a specific capacity as high as 596.69 C g^{-1} at 1 A g^{-1}, and cycling retention of 80.4% after 3000 cycles at 10 A g^{-1}. Furthermore, the MXene-$NiCo_2S_4$@NF as a binder-free electrode could be applied to the asymmetric solid-state capacitors (ASC) without further treatment.

Experimental Section

1. Fabrication of Ti_3C_2 MXene electrodes

The $Ti_3C_2T_x$ was synthesized and intercalated by hydrofluoric acid (HF) etching and dimethyl

6

sulfoxide (DMSO) intercalation, as described in reported works.[27, 28] The obtained $Ti_3C_2T_x$ has been denoted as "in-$Ti_3C_2T_x$". Then, a colloidal suspension of $Ti_3C_2T_x$ was prepared by mixing 0.1 g of the in-Ti_3C_2 powder with 100 mL of de-ionize water under vigorous magnetic stirring for 4 h. Next, NF was cut into the required size (1×1 cm), and the surface was cleaned with alcohol. The $Ti_3C_2T_x$ colloidal suspension was then dropped with a pipette onto the pretreated NF sheet, which was placed on a hotplate maintained at 80 ℃. The $Ti_3C_2T_x$ content of the whole electrode was easily controlled by adjusting the volume of the suspension.

2. Synthesis of NiCo2S4 nanosheets on Ti3C2Tx MXene electrodes

Our synthesis procedure involved two steps: co-electrodeposition of mixed metal (Ni, Co) hydroxide precursor followed by a vapor-phase hydrothermal method. First, the bimetallic layered double hydroxides (LDHs) were electrochemically deposited onto the $Ti_3C_2T_x$ MXene electrodes in a 4 mM Co $(NO_3)_2$ $6H_2O$ and 2 mM Ni$(NO_3)_2$ $6H_2O$ solution at room temperature. The $Ti_3C_2T_x$ MXene electrodes served as the working electrodes, the saturated Ag/AgCl served as the reference electrode, and a Pt sheet served as the counter electrode. The deposition was performed using a cyclic voltammetry (CV) electrodeposition method. The potential ranged from -1.2 to 0.2 V at 5 mV^{-1} per cycle. Second, the precursors were placed in a 50 mL Teflon-lined stainless-steel autoclave with 35 mL of sodium sulfide solution (0.2 M) and kept at 120 ℃ for 14 h. Finally, the products were collected via washing with DI water and ethanol, followed by drying at 60 ℃ for 12 h to obtain the MXene-NiCo2S4 electrodes.

3. Fabrication of ASC devices

The ASC devices were fabricated in a two-electrode configuration, using the as-prepared products as the positive electrode and active carbon (AC) as the negative electrode, with a poly(vinyl alcohol) (PVA)–KOH polymer electrolyte separator between them. The AC electrode was prepared by mixing 80 wt.% active materials, 10 wt.% acetylene black, and 10 wt.% polytetrafluoroethylene.

The PVA–KOH polymer electrolyte was prepared via the typical process, which is described as follows: First, 6 g of PVA was dissolved in 60 mL of DI water with stirring for 2 h at 85 °C. Then, 3 g of KOH was dissolved in 20 mL of DI water. Finally, the two resulting solutions were mixed at 80 °C with vigorous stirring until the mixture became clear. Next, they were immersed in the PVA–KOH solution for 8 min. After evaporation of the excess water at room temperature, the two electrodes were assembled. The final ASC device was obtained after the solidification of the PVA–KOH gel.

4. Characterization

The crystalline structure and phase purity of the products were examined via X-ray diffraction (XRD) analysis using a D8 Advance (Germany, Bruker) automated X-ray diffractometer system with Cu-Kα (λ = 1.5418 Å) radiation at 40 kV and 40 mA in the 2θ range of 5° to 90° at room temperature. The structure and morphology of the samples were characterized via X-ray photoelectron spectroscopy (XPS; Al Kα excitation laser, ESCA2000), field-emission scanning electron microscopy (SEM) and high-resolution transmission electron microscopy

8

(HRTEM) (JEM-2100F).
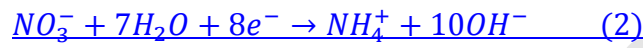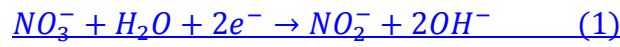
5. Electrochemical measurements

Electrochemical experiments were performed in 3 M KOH using a three-electrode electrochemical workstation (RST 5100F). A Pt plate and Hg/HgO electrode were used as counter and reference electrodes, respectively, while the MXene/NiCo$_2$S$_4$ electrodes were used directly as the working electrode. The CV curves were measured in the potential window of 0–0.6 V at 5, 10, 30, 50, 70, and 100 mVs^{-1} and the galvanostatic charge-discharge (GCD) process was conducted in the potential range of 0–0.55 V at 1, 2, 6, and 10 Ag^{-1}.

An ASC device was assembled using MXene-NiCo$_2$S$_4$@NF as the positive electrode, AC@NF as the negative electrode, and the PVA–KOH gel electrolyte between them. The mass loading for the negative electrode was determined by balancing the charges stored in the two electrodes. Generally, the charges stored by the positive and negative electrodes can be determined as follows: $Q_+ = Q_-$, where $Q_+ = C_+ \times \Delta V \times m_+$ and $Q_- = C_- \times \Delta V \times m_-$. In this study, the mass loading of the positive and negative electrodes was 1.2 and 5.7 mg, respectively.

Results and Discussion

The fabrication process for the MXene-NiCo$_2$S$_4$@NF electrode is described in Figure 1. First, Ti$_3$C$_2$T$_X$ was synthesized by etching Ti$_3$AlC$_2$ using HF, followed by mixing with DMSO for the intercalation of Ti$_3$C$_2$T$_X$. Then, the Ti$_3$C$_2$T$_x$-based electrode was fabricated by a simple dropping and drying method with the clay nature of MXene, followed by the deposition of

9

nickel-cobalt LDHs on the MXene@NF electrode using electrodeposition via electrostatic interaction.[40] *The preparation of LDHs based on Ni^{2+} and Co^{3+} by electrodeposition is usually carried out in a solution containing the nitrates of the bivalent and trivalent ions, and applying a cathodic potential to the electrode to promote the reduction of nitrates and water molecules. The reactions either consume H^+ or produce OH^- ions near the electrode surface, thus increasing the local pH and precipitation of the LDH, as shown in the following equations (1-3).[41]*

$$NO_3^- + H_2O + 2e^- \rightarrow NO_2^- + 2OH^- \qquad (1)$$

$$NO_3^- + 7H_2O + 8e^- \rightarrow NH_4^+ + 10OH^- \qquad (2)$$

$$xNi^{2+} + 2xCo^{2+} + 6xOH^- \rightarrow Ni_xCo_{2x}(OH)_{6x} \quad (3)$$

Subsequently, the composite electrode was mixed with $Na_2S \cdot 9H_2O$ via the hydrothermal method. The Na_2S as a sulfur source was exposed to hydrolysis, producing active sulfide ions (S^{2-}) and causing the nucleation of the $NiCo_2S_4$ crystal via an anion-exchange reaction. During the sulfidation process, the S^{2-} anions would donate two electrons to Ni and Co ions in the LDH, followed by the exchange with OH^- anions in the solution (equation 4).[34]

$$Ni_xCo_{2x}(OH)_{6x} + 4xS^{2-} \rightarrow xNiCo_2S_4 + 6xOH^- + 2xe^- \quad (4)$$
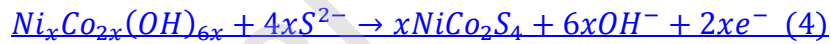
As the reaction progressed, thin $NiCo_2S_4$ nanoflakes were deposited on the surface of MXene. To investigate the variations in the electrochemical properties, according to changes in quantity of drops of the $Ti_3C_2T_x$ suspension and the electrodeposition times under the unified experimental conditions, we prepared several samples with different mass fractions of MXene in the active materials. These were denoted as 0-MXene-$NiCo_2S_4$@NF, 50-MXene-$NiCo_2S_4$@NF, 60-MXene-$NiCo_2S_4$@NF, 70-MXene-$NiCo_2S_4$@NF, and 100-MXene-$NiCo_2S_4$@NF corresponding to approximately 0% (pure $NiCo_2S_4$ electrode), 50%, 60%, 70%, and 100% (pure MXene electrode), respectively. The mass-loading of MXene and $NiCo_2S_4$ on

the NF is shown in Table S1.

The XRD patterns of the as-synthesized samples of MXene and MXene-NiCo$_2$S$_4$ are shown in Figure 2a. The MXene-NiCo$_2$S$_4$ sample exhibits (002), (004), (008), and (110) peaks, corresponding to the 2θ values of typical Ti$_3$C$_2$. The full width at half maximum (FWHM) of the (002) diffraction peak increases and the peak shifts to a lower angle, indicating that the DMSO molecules have entered the interlayer of MXene, successfully enlarged the c-lattice parameters of the MXene nanosheets, as well as increased the interlayer spacing of the nanosheets, promoting the adsorption of the metal cations during the electrodeposition process. Additionally, the XRD pattern shows high-intensity diffraction peaks at 2θ values of 31.5°, 38.3°, 50.5°, and 55.3°, which are readily attributed to the (311), (400), (511), and (440) reflections, respectively, indexed to the cubic-type NiCo$_2$S$_4$ phase (JCPDS No. 43-1477), indicating the good crystallinity of the composite. However, compared with the standard JCPDS card, the (440) peak is slightly shifted toward a smaller angle and a similar cubic Co$_3$S$_4$ phase (JCPDS No. 42-1448), confirming the substitution of Co ions by Ni ions, which slightly changed the lattice parameters while maintaining the crystal structure.[42]
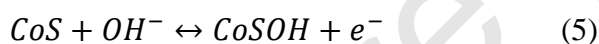
To investigate the surface chemical state of the MXene-NiCo$_2$S$_4$ sample, XPS was performed, as shown in Figure 2b. The Ti 2p and C 1s elemental spectra are shown in the Supporting Information (Figures S1a and b, respectively). The Ni 2p spectrum (Figure 2c) was fitted with two spin-orbit doublets and two shakeup satellites (marked as "Sat.") using the Gaussian fitting method. The strong peaks at 874.3 eV for Ni 2p$_{3/2}$ and 856.0 eV for Ni 2p$_{1/2}$ indicate the co-existence of Ni^{2+} and Ni^{3+}.[43] The spectrum of the S 2p region is shown in Figure 2d. The binding energies at 161.8 and 163.1 eV correspond to 2p$_{3/2}$ and 2p$_{1/2}$, respectively, indicating

11

the presence of the $NiCo_2S_4$ and MXene in the compound without any impurities such as oxidized $NiCo_2O_4$, as well as the presence of Ni^{2+}/Ni^{3+} and Co^{2+}/Co^{3+} ions as abundant active sites for the redox reaction, which are responsible for the electrochemical performance of the electrode.[44, 45]

The SEM and transmission electron microscopy (TEM) images in Figures 3 and S2 show the surface morphologies of the pure MXene and MXene-$NiCo_2S_4$. Figure S2 demonstrates the delamination of Ti_3C_2 before and after the DMSO treatment, indicating the increase in the interlayer spacing, which facilitated the intercalation of the ions. Figures 3a and b show the morphology of the cross-section and side-section of the composite nanosheets. Compared with the pure MXene (insets of Figures 3a and b), the monolayer lamellae and surface roughness of the composite clearly increased after electrodeposition and sulfuration. Moreover, as shown in Figure 3c, the edge of the MXene was evidently wrapped in fibrous $NiCo_2S_4$ nanoflakes, which significantly increased the volume of each nanoparticle. As mentioned previously, the MXene-$NiCo_2S_4$ nanosheets exhibited a larger surface area and volume than the pure MXene, increasing the contact area of the composite with the electrolyte, which allows a shorter ion diffusion distance and gives rise to more active sites for the Faradaic redox reaction. Furthermore, according to the HRTEM and selected-area electron diffraction (SAED) results shown in Figure 3d, the interplanar spacing was evaluated as 0.23 nm, which agrees well with the (400) lattice plane of spinel $NiCo_2S_4$. The SAED pattern is also consistent with the XRD results, and the diffraction rings indicate the growth of $NiCo_2S_4$ on the surface of the MXene.[46]

The CV and GCD measurements were performed using a three-electrode system to evaluate

the electrochemical properties of the $NiCo_2S_4$ grown on the MXene@NF as a binder-free electrode. Figures 4a, b, and S3 show the CV and GCD curves of the MXene-$NiCo_2S_4$@NF electrodes with different mass ratios. *Notably, one pair of distinct redox peaks in the CV curves and the charge–discharge plateaus in the GCD curves can be easily distinguished, which are mainly caused by the reversible Faradaic reactions on the surface or near-surface of the active materials, clearly demonstrating the typical battery-type behavior of the MXene-$NiCo_2S_4$ composite.[47-49]* Figure 4a shows the CV curves at different scan rates ranging from 0–100 mV s^{-1} in a potential window of 0 to 0.55 V. These redox peaks are attributed to the reversible Faradaic redox reactions of $Co^{2+}/Co^{3+}/Co^{4+}$ and Ni^{2+}/Ni^{3+} based on the following equations (5–7).[43, 50]

$$CoS + OH^- \leftrightarrow CoSOH + e^- \qquad (5)$$

$$CoSOH + OH^- \leftrightarrow CoSO + H_2O + e^- \qquad (6)$$

$$NiS + OH^- \leftrightarrow NiSOH + e^- \qquad (7)$$

The single component of $NiCo_2S_4$ in the KOH electrolyte is responsible for the charge storage of the composite electrode. Moreover, with the increase in the scan rate, the anodic and cathodic peaks showed a significant shift toward the positive and negative potentials, respectively. Moreover, a change is observed in the intensity of the peak currents, indicating an increase in the chemical composition polarization and internal resistance with the increase in the scan rate; this results in the lagging kinetics during the charge transfer process. Additionally, the OH$^-$ ions in the alkaline electrolyte play a vital role in the electrochemical oxidation and reduction of nickel or cobalt sulfides, as described in previous studies.[51-53]

As well known, rate capability is a crucial parameter for the potential application of the ECs.

Therefore, we performed GCD measurements against a Pt plate as a counter electrode and Hg/HgO as a reference electrode at different current densities between 1 and 10 A g⁻¹. *The voltage plateaus at 0.4−0.5 V for the charge curves and 0.4−0.3 V for the discharge curves are consistent with the redox reactions observed in the CV curves. In addition, the GCD curves of the MXene-NiCo₂S₄@NF electrode are symmetrical without an obvious voltage drop at low current densities, indicating a rapid current−voltage response and excellent electrochemical reversibility.[42]* According to the calculations based on equation (4), the MXene-NiCo₂S₄@NF exhibited excellent specific capacity and rate capability with increasing current density.[54]

$$C_s = \frac{I\Delta t}{m} \quad (4)$$

where C_s (C g⁻¹), I (mA), m (mg), and Δt (s) represent the specific capacity, discharge current, mass of the active material, and total discharge time, respectively.

The 60-MXene-NiCo₂S₄@NF sample exhibited an excellent specific capacity, with values of 596.69, 488.46, 333.73, and 288.14 C g⁻¹ (1147.47, 939.35, 641.79, and 554.04 F g⁻¹) at 1, 2, 6, and 10 A g⁻¹ respectively, and the retention ratio was maintained at 48.3% at 10 A g⁻¹. As shown in Figure 3c, although the C_s of the 100-MXene-NiCo₂S₄@NF (pure MXene) electrode decreased only from 106.34 C g⁻¹ (at 1 A g⁻¹) to 78.47 C g⁻¹ with a high retention rate of 73.7%. It has a low specific capacity, which limits its application for supercapacitors. The 0-MXene-NiCo₂S₄@NF (pure NiCo₂S₄) electrode shows a higher capacity, but its lower retention rate at a high current density also limits its application. The improved electrochemical properties of the MXene-NiCo₂S₄ samples were mostly due to the suitable design of the microstructure. Compared with the pure MXene and pure NiCo₂S₄, our samples, which depended on the

14

MXene as a substructure that guaranteed a large surface area and improved the conductivity, exhibited excellent performance, owing to the unique layered structure and extraordinary characteristics of titanium and carbon. Additionally, $NiCo_2S_4$ enhanced the specific capacity in the alkaline electrolyte owing to the reversible and rapid redox reactions, which are attributed to the activity of Ni^{2+}/Ni^{3+} and $Co^{2+}/Co^{3+}/Co^{4+}$ during the charge-discharge process.

Electrochemical impedance spectroscopy (EIS) was performed to investigate the resistance and ion transport in the different electrodes over the frequency range of 0.01–100 kHz (Figure S4): In the high-frequency range, the intercept of the semicircular curve on the real axis (Z_0) represents the equivalent series resistance (ESR), which includes the electrolyte resistance, ohmic resistance of the active materials, and contact resistance at the interface between the active materials and the substructure. The ESR value of the MXene-$NiCo_2S_4$@NF electrode was 0.26 Ω, which is far lower than that of pure $NiCo_2S_4$ (0.37 Ω). The semicircle curve corresponds to the double-layer capacitance (C_{dl}), and the radius reveals the charge-transfer resistance (R_{ct}) involved in the Faradaic reaction at the interface between the electrode and electrolyte.[55] In the low-frequency range, the slope of the straight line represents the Warburg resistance, which is more inclined to the vertical, indicates the characteristic feature of capacitive behavior.[56] According to the data shown in Table S1, the composite electrode exhibited higher conductivity than pure $NiCo_2S_4$ because of the MXene, which significantly reduced the internal resistance and improved the charge-transfer conductivity. Additionally, the three-dimensional (3D) structure minimized the contact impedance between the active materials and the electrolyte.[57]

The GCD characterization of the cycling stability of the 60-MXene-NiCo$_2$S$_4$ and 0-MXene-

NiCo$_2$S$_4$ (pure NiCo$_2$S$_4$) electrodes at 10 A g^{-1} for serval cycles is shown in Figure 4d. The early

upsurge in the specific capacity was due to the activation of active materials in the early cycles.

After 3000 cycles, the discharge capacity of the 60-MXene-NiCo$_2$S$_4$ is observed to remain at

80.4%, which is significantly higher than that of the pure NiCo$_2$S$_4$ electrode (61.2% after 2000

cycles), as well as other previously studied sulfide- (80% after 1000 cycles) and LDH- (65%

after 3000 cycles) based materials.[58, 59] During the continuous charge-discharge cycles, the

active materials underwent significant structural degradation, as indicated by the SEM image

(inset). Compared with Figures 3a and b (original sample), the interlayer structure of the

MXene particles was maintained even after 3000 cycles implying that MXene effectively

suppressed the agglomeration of the TMSs, leading to better cycling stability.

To investigate the capacitive performance of the MXene-NiCo2S4 electrode, an ASC device

employing the AC@NF and MXene-NiCo2S4@NF as negative and positive electrodes,

respectively, was fabricated. The pre-fabricated PVA−KOH electrolyte (gel) was used as a

separator between the negative and positive electrodes, as shown in Figure 5a. Furthermore,

Figure S5a displays the CV curves of AC (-1 ~ 0 V) and MXene-NiCo$_2$S$_4$ (0 ~ 0.6 V) single

electrodes measured at a scan rate of 5 mV s^{-1} with a three-electrode system. Based on the CV

curves of each single electrode, the voltage range of the ASC device was evaluated from 0 to

1.6 V, which achieved higher energy and power densities.[48] The shapes of the CV curves of

the device did not noticeably change with the increase in the scan rate from 5 to 100 mV s^{-1},

indicating the fast charge-discharge behavior of the capacitor. The GCD curves of the ASC at

different current densities are illustrated in Figure 5c. According to the discharge curves, the

16

energy density (E) and power density (P) were calculated using equations (5-6):

$$E = \frac{1}{2}CV^2 \qquad (5)$$

$$P = \frac{E}{\Delta t} \qquad (6)$$

where V (V), E (Wh kg^{-1}), P (W kg^{-1}), and Δt represent the voltage excluding the initial voltage loss, energy density, average power density, and discharge time, respectively.

According to the specific capacity values, the energy density of the MXene-NiCo$_2$S$_4$@NF//AC@NF was calculated as 27.24, 25.43, 18.82, and 11.87 Wh kg^{-1} at power densities of 0.48, 0.97, 1.65, and 3.38 kW kg^{-1}, respectively. These results indicate our ASC device produced higher energy density than the previously reported devices such as CoSx//GR (14.7 Wh kg^{-1} at 369 W kg^{-1}),[60] Ni$_2$S$_3$@CNT//AC (19.8 Wh kg^{-1} at 798 W kg^{-1}),[61] NiCo$_2$S$_4$//C (22.8 Wh kg^{-1} at 160 W kg^{-1}),[62] Ni$_x$Co$_{1-x}$ LDH@ZTO heterostructure//AC (23.7 Wh kg^{-1} at 284.2 W kg^{-1}),[63] NiCo$_2$O$_4$@NiMoO$_4$//AC (21.7 Wh kg^{-1} at 157 W kg^{-1}),[64] and NiCo$_2$S$_4$-CFP//AC (17.3 Wh kg^{-1} at 200 W kg^{-1}),[65] as summarized in Figure 5d. To further demonstrate its practical applicability, we applied the ASC device to a commercial light-emitting diode (LED), as displayed in Figures S5b–e.

The superior supercapacitive performance of the MXene-NiCo$_2$S$_4$@NF//AC@NF ASC device originates from the following characteristics: (1) MXene, as an ideal matrix, provides a highly rapid path for fast electron transport owing to the outstanding conductivity of the carbide materials; (2) The NiCo$_2$S$_4$ nanosheets enhance the interfacial contact between the electrolyte and the active materials, as well as provide abundant active sites for energy storage properties; (3) The AC@NF negative electrode facilitates ion transport and electrolyte accessibility, leading to lower resistance.

17

Conclusions

In conclusion, we fabricated a novel 3D MXene-NiCo$_2$S$_4$ nanostructure as a binder-free electrode for chemical capacitors. The proposed structure not only overcame the low specific capacitance of MXene but also improved the weak cycling stability and low conductivity of TMS. First, the MXene clay was synthesized and affixed on NF without a binder which effectively reduced the internal resistance and accelerated charge transport. Then, the precursor was electrodeposited on the surface of the MXene nanosheets, to which sodium sulfide nonahydrate was added, followed by sulfuration via the hydrothermal method through an anion-exchange reaction. The fabricated MXene-NiCo$_2$S$_4$ electrode exhibited excellent electrochemical performance, with a high specific capacity (596.69 C g^{-1} at 1 A g^{-1}) and outstanding cycling stability (retained 80% of the initial capacity after 3000 cycles). The cycling stability was mostly due to the unique nanostructure of the titanium carbide substructure, which not only provided a large surface area but also withstood the volumetric strain due to the application of charges along with the redox reaction. Furthermore, an ASC device assembled with MXene-NiCo$_2$S$_4$ as a positive electrode and AC as a negative electrode exhibited a high energy density of 27.2 Wh kg^{-1} and a high power density of 0.48 kW kg^{-1}. The results indicate that the proposed 3D nanostructure can improve the performance of supercapacitors and other energy-storage devices.

Acknowledgment

References

[1] Y. Zhu, S. Murali, M.D. Stoller, K. Ganesh, W. Cai, P.J. Ferreira, A. Pirkle, R.M. Wallace, K.A. Cychosz, M. Thommes, science, 332 (2011) 1537-1541.

[2] P. Simon, Y. Gogotsi, B. Dunn, Science, 343 (2014) 1210-1211.

[3] S. Chen, J. Zhu, X. Wu, Q. Han, X. Wang, ACS nano, 4 (2010) 2822-2830.

[4] D. Pech, M. Brunet, H. Durou, P. Huang, V. Mochalin, Y. Gogotsi, P.-L. Taberna, P. Simon, Nature nanotechnology, 5 (2010) 651.

[5] S.S. Shankar, R.M. Shereema, R.B. Rakhi, ACS applied materials & interfaces, 10 (2018) 43343-43351.

[6] S. Zhu, L. Li, J. Liu, H. Wang, T. Wang, Y. Zhang, L. Zhang, R.S. Ruoff, F. Dong, ACS nano, 12 (2018) 1033-1042.

[7] W. Xu, K. Zhao, W. Huo, Y. Wang, G. Yao, X. Gu, H. Cheng, L. Mai, C. Hu, X. Wang, Nano Energy, 62 (2019) 275-281.

[8] L.L. Zhang, X. Zhao, Chemical Society Reviews, 38 (2009) 2520-2531.

[9] P. Simon, Y. Gogotsi, World Scientific, 7 (2010) 320-329.

[10] Y. Wang, Z. Shi, Y. Huang, Y. Ma, C. Wang, M. Chen, Y. Chen, The Journal of Physical Chemistry C, 113 (2009) 13103-13107.

[11] Z. Yu, L. Tetard, L. Zhai, J. Thomas, Energy & Environmental Science, 8 (2015) 702-730.

[12] W. Xu, J. Lu, W. Huo, J. Li, X. Wang, C. Zhang, X. Gu, C. Hu, Nanoscale, 10 (2018) 14304-14313.

[13] C. Xiong, T. Li, A. Dang, T. Zhao, H. Li, H. Lv, Journal of Power Sources, 306 (2016) 602-610.

[14] C. Xiong, T. Li, T. Zhao, A. Dang, X. Ji, H. Li, M. Etesami, Nano, 13 (2018) 1850013.

[15] C. Xiong, B. Li, X. Lin, H. Liu, Y. Xu, J. Mao, C. Duan, T. Li, Y. Ni, Composites Part B: Engineering,165 (2018) 10-46.

[16] M. Naguib, M. Kurtoglu, V. Presser, J. Lu, J. Niu, M. Heon, L. Hultman, Y. Gogotsi, M.W. Barsoum, Advanced Materials, 23 (2011) 4248-4253.

[17] A. Lipatov, H. Lu, M. Alhabeb, B. Anasori, A. Gruverman, Y. Gogotsi, A. Sinitskii, Science Advances, 4 (2018) 485-491.

[18] S. Zhao, H.-B. Zhang, J.-Q. Luo, Q.-W. Wang, B. Xu, S. Hong, Z.-Z. Yu, ACS nano, 12 (2018) 11193-11202.

[19] M.R. Lukatskaya, O. Mashtalir, C.E. Ren, Y. Dall'Agnese, P. Rozier, P.L. Taberna, M. Naguib, P. Simon, M.W. Barsoum, Y. Gogotsi, Science, 341 (2013) 1502-1505.

[20] M. Ghidiu, J. Halim, S. Kota, D. Bish, Y. Gogotsi, M.W. Barsoum, Chemistry of Materials, 28 (2016) 3507-3514.

[21] M.-Q. Zhao, M. Torelli, C.E. Ren, M. Ghidiu, Z. Ling, B. Anasori, M.W. Barsoum, Y. Gogotsi, Nano Energy, 30 (2016) 603-613.

[22] B. Ahmed, D.H. Anjum, Y. Gogotsi, H.N. Alshareef, Nano Energy, 34 (2017) 249-256.

[23] B. Anasori, M.R. Lukatskaya, Y. Gogotsi, Nature Reviews Materials, 2 (2017) 16098.

[24] Y. Dong, S. Zheng, J. Qin, X. Zhao, H. Shi, X. Wang, J. Chen, Z.S. Wu, ACS nano, 12 (2018) 2381-2388.

[25] M.R. Lukatskaya, S. Kota, Z. Lin, M.-Q. Zhao, N. Shpigel, M.D. Levi, J. Halim, P.-L. Taberna, M.W. Barsoum, P. Simon, Nature Energy, 2 (2017) 17105.

[26] A. VahidMohammadi, M. Mojtabavi, N.M. Caffrey, M. Wanunu, M. Beidaghi, Advanced Materials, 8 (2018) 1806931.

[27] O. Mashtalir, M. Naguib, V.N. Mochalin, Y. Dall'Agnese, M. Heon, M.W. Barsoum, Y. Gogotsi, Nature communications, 4 (2013) 1716.

[28] M. Hu, Z. Li, H. Zhang, T. Hu, C. Zhang, Z. Wu, X. Wang, Chemical Communications, 51 (2015) 13531-13533.

[29] R.B. Rakhi, B. Ahmed, D. Anjum, H.N. Alshareef, ACS applied materials & interfaces, 8 (2016) 18806-18814.

[30] Q.X. Xia, J. Fu, J.M. Yun, R.S. Mane, K.H. Kim, Rsc Advances, 7 (2017) 11000-11011.

[31] M. Zhu, Y. Huang, Q. Deng, J. Zhou, Z. Pei, Q. Xue, Y. Huang, Z. Wang, H. Li, Q. Huang, Advanced Energy Materials, 6 (2016) 1600969.

[32] M. Boota, B. Anasori, C. Voigt, M.Q. Zhao, M.W. Barsoum, Y. Gogotsi, Advanced Materials, 28 (2016) 1517-1522.

[33] R. Liu, M. Miao, Y. Li, J. Zhang, S. Cao, X. Feng, ACS applied materials & interfaces, 10 (2018) 44787-44795.

[34] L. Shen, J. Wang, G. Xu, H. Li, H. Dou, X. Zhang, Advanced Energy Materials, 5 (2015) 1400977.

[35] B. Gao, X. Li, K. Ding, C. Huang, Q. Li, P.K. Chu, K. Huo, Journal of Materials Chemistry A, 7 (2019) 14-37.

[36] A. Sajedi-Moghaddam, E. Saievar-Iranizad, M. Pumera, Nanoscale, 9 (2017) 8052-8065.

[37] Z. Fan, Y. Wang, Z. Xie, D. Wang, Y. Yuan, H. Kang, B. Su, Z. Cheng, Y. Liu, Advanced Science, 5 (2018) 1800750.

[38] K.S. Kumar, N. Choudhary, Y. Jung, J. Thomas, ACS Energy Letters, 3 (2018) 482-495.

[39] X. Chen, H.-J. Peng, R. Zhang, T.-Z. Hou, J.-Q. Huang, B. Li, Q. Zhang, ACS Energy Letters, 2 (2017) 795-801.

[40] H. Li, F. Musharavati, E. Zalenezhad, X. Chen, K. Hui, K. Hui, Electrochimica Acta, 261 (2018) 178-187.

[41] I. Gualandi, M. Monti, E. Scavetta, D. Tonelli, V. Prevot, C. Mousty, Electrochimica Acta, 152 (2015) 75-83.

[42] H. Chen, J. Jiang, L. Zhang, H. Wan, T. Qi, D. Xia, Nanoscale, 5 (2013) 8879-8883.

[43] J. Pu, F. Cui, S. Chu, T. Wang, E. Sheng, Z. Wang, ACS Sustainable Chemistry & Engineering, 2 (2013) 809-815.

[44] D. Li, Y. Gong, C. Pan, Scientific reports, 6 (2016) 29788.

[45] W. Liu, H. Niu, J. Yang, K. Cheng, K. Ye, K. Zhu, G. Wang, D. Cao, J. Yan, Chemistry of Materials, 30 (2018) 1055-1068.

[46] X. He, Q. Liu, J. Liu, R. Li, H. Zhang, R. Chen, J. Wang, Chemical Engineering Journal, 325 (2017) 134-143.

[47] T. Brousse, D. Bélanger, J.W. Long, Journal of The Electrochemical Society, 162 (2015) A5185-A5189.

[48] Y. Gogotsi, R.M. Penner, in Energy storage in nanomaterials–capacitive, pseudocapacitive, or battery-like?, ACS nano 12 (2018) 2081-2083.

[49] M. Salanne, B. Rotenberg, K. Naoi, K. Kaneko, P.-L. Taberna, C.P. Grey, B. Dunn, P. Simon, Nature Energy, 1 (2016) 16070.

[50] L. Shen, J. Wang, G. Xu, H. Li, H. Dou, X. Zhang, Advanced Energy Materials, 5 (2015) 1400977.

[51] L. Zhang, H.B. Wu, X.W.D. Lou, Chemical communications, 48 (2012) 6912-6914.

[52] Y. Gao, S. Chen, D. Cao, G. Wang, J. Yin, Journal of Power Sources, 195 (2010) 1757-1760.

[53] J. Fu, L. Li, J.M. Yun, D. Lee, B.K. Ryu, K.H. Kim, Chemical Engineering Journal, 375 (2019) 121939.

[54] Z. Pan, F. Cao, X. Hu, X. Ji, Journal of Materials Chemistry A, 7 (2019) 8984-8992.

[55] Q. Qin, L. Chen, T. Wei, X. Liu, Small, 15 (2018) 1803639.

[56] Z. Weng, Y. Su, D.W. Wang, F. Li, J. Du, H.M. Cheng, Advanced Energy Materials, 1 (2011) 917-922.

[57] W. Chen, C. Xia, H.N. Alshareef, ACS nano, 8 (2014) 9531-9541.

[58] H. Li, F. Musharavati, J. Sun, F. Jaber, E. Zalnezhad, K. Hui, K. Hui, Journal of The Electrochemical Society, 165 (2018) A407-A415.

[59] W. Yu, W. Lin, X. Shao, Z. Hu, R. Li, D. Yuan, Journal of Power Sources, 272 (2014) 137-143.

[60] D.P. Dubal, G.S. Gund, C.D. Lokhande, R. Holze, Energy Technology, 2 (2014) 401-408.

[61] C.-S. Dai, P.-Y. Chien, J.-Y. Lin, S.-W. Chou, W.-K. Wu, P.-H. Li, K.-Y. Wu, T.-W. Lin, ACS applied materials & interfaces, 5 (2013) 12168-12174.

[62] W. Kong, C. Lu, W. Zhang, J. Pu, Z. Wang, Journal of Materials Chemistry A, 3 (2015) 12452-12460.

[63] X. Wang, A. Sumboja, M. Lin, J. Yan, P.S. Lee, Nanoscale, 4 (2012) 7266-7272.

[64] D. Cheng, Y. Yang, J. Xie, C. Fang, G. Zhang, J. Xiong, Journal of Materials Chemistry A, 3 (2015) 14348-14357.

[65] X. Xiong, G. Waller, D. Ding, D. Chen, B. Rainwater, B. Zhao, Z. Wang, M. Liu, Nano Energy, 16 (2015) 71-80.
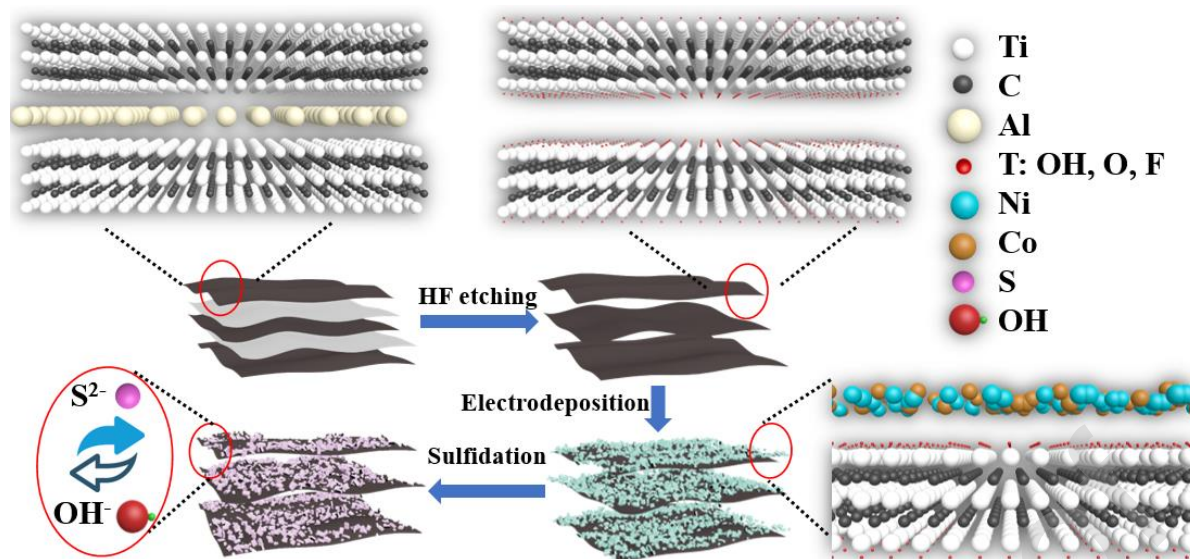
Figure 1. Schematic of the fabrication process for the MXene-NiCo$_2$S$_4$ electrode.
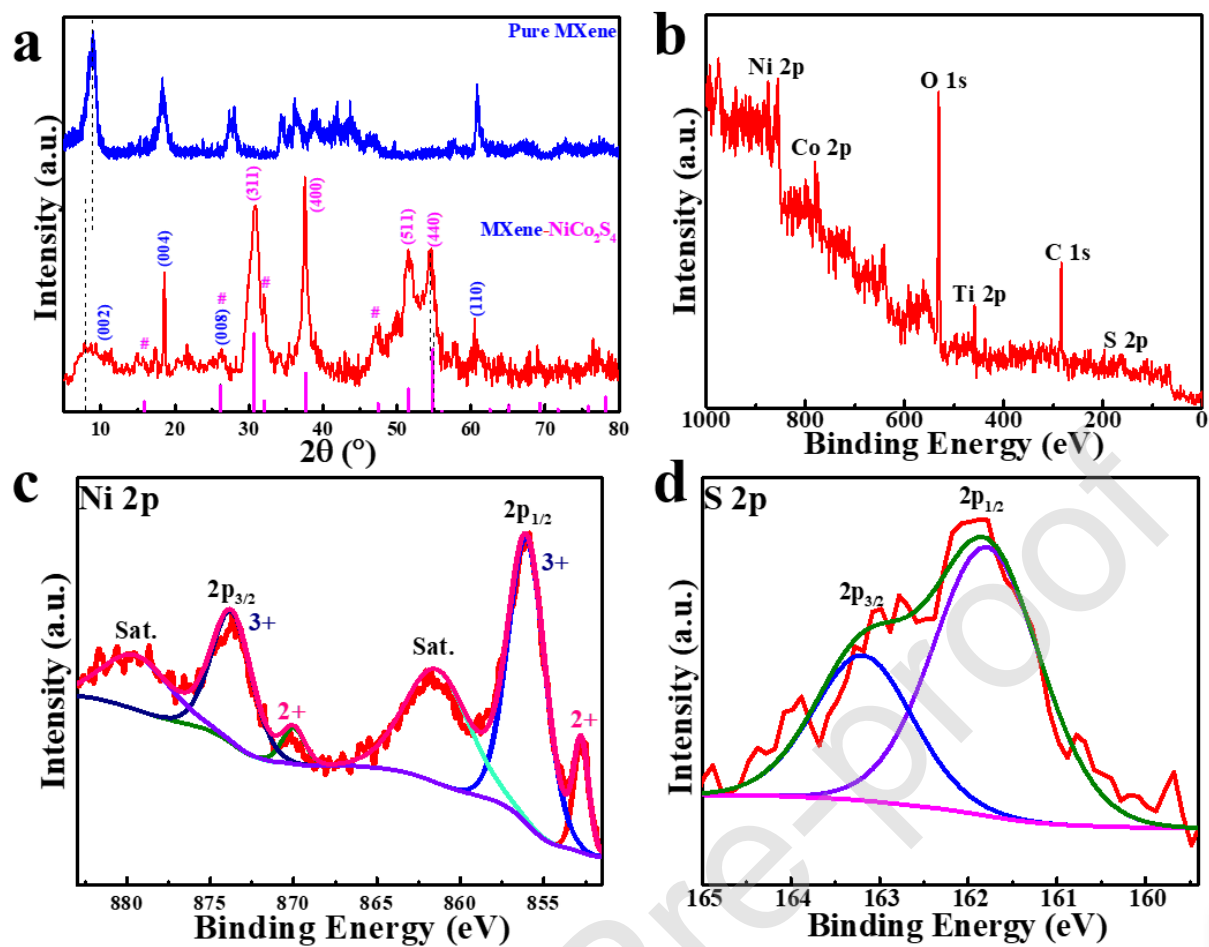
Figure 2. (a) XRD pattern and (b) XPS survey spectra of MXene-NiCo$_2$S$_4$; (c, d) core-level spectra of the Ni 2p and S 2p regions, respectively.
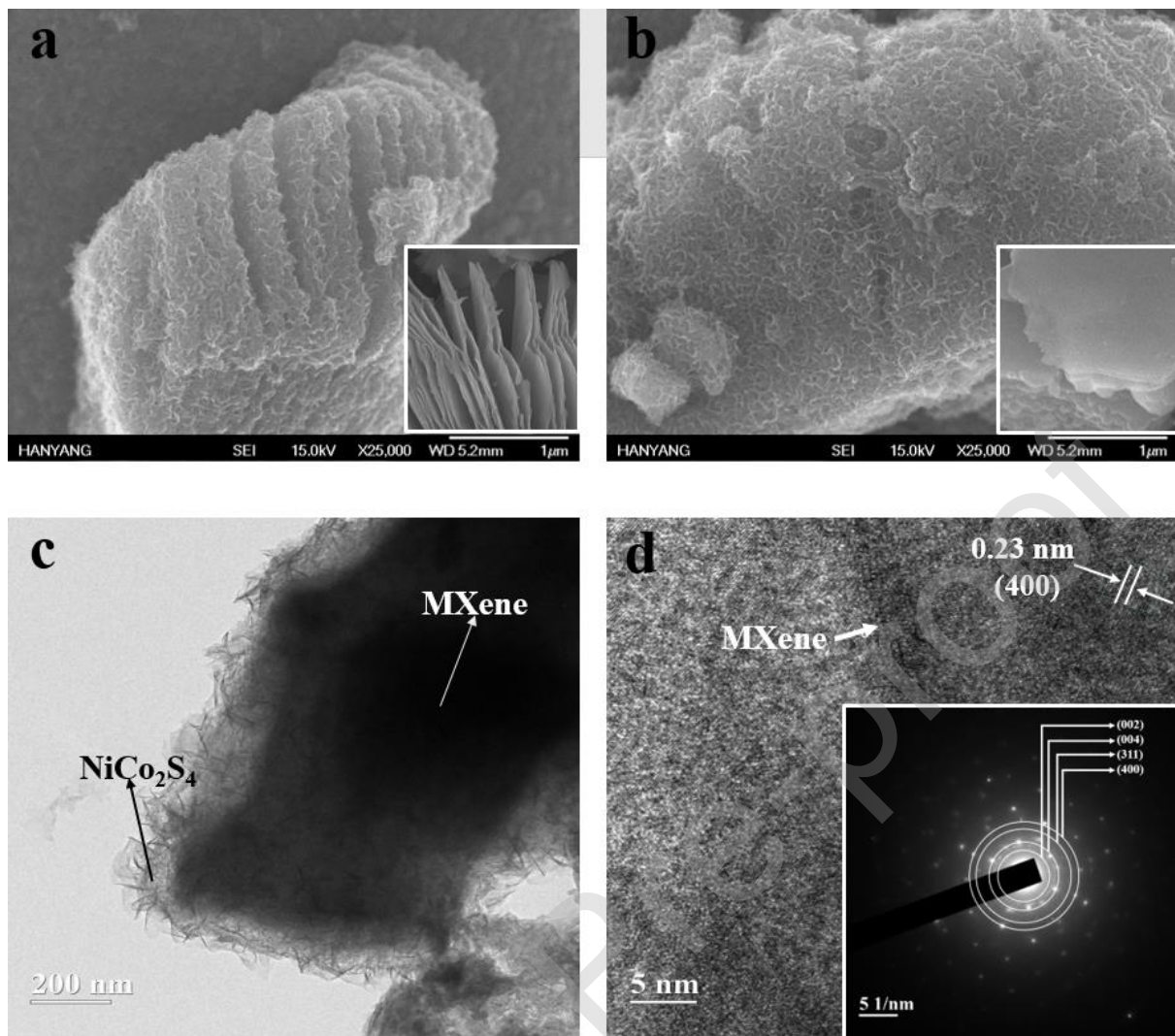
Figure 3. (a, b) SEM (insets of (a) and (b) show intercalated MXene) and (c, d) TEM images of the MXene-NiCo$_2$S$_4$ electrode at different magnifications. The inset of (d) shows the SAED pattern.
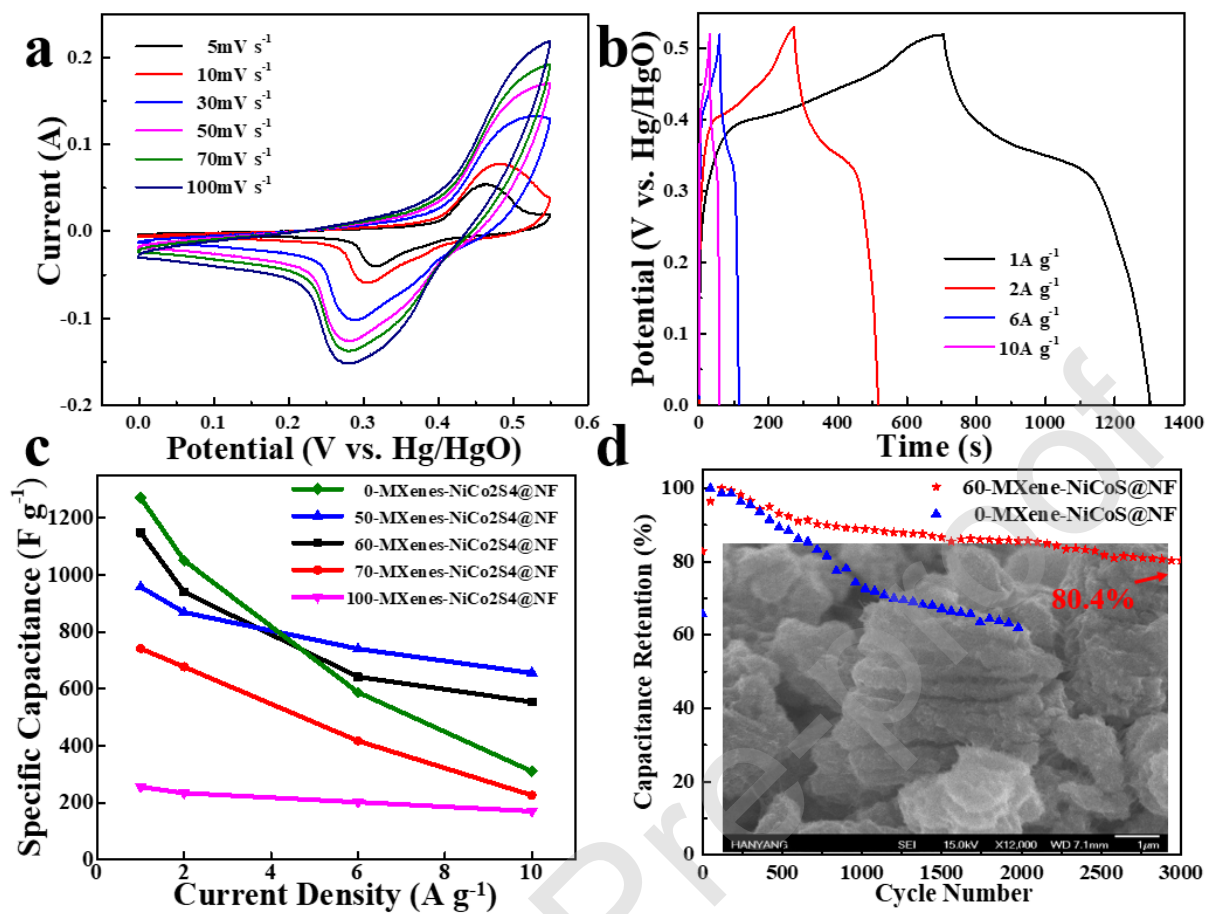
Figure 4. (a) CV curves and (b) GCD curves of the 60-MXene-NiCo$_2$S$_4$@NF electrode at different scan rates and different current densities; (c) specific capacity of MXene, NiCo$_2$S$_4$, and different ratios of MXene-NiCo$_2$S$_4$; *(d) cycling stability of the 60-MXene-NiCo$_2$S$_4$@NF electrode and 0-MXene-NiCo$_2$S$_4$@NF electrode at 10 A g^{-1} for several cycles and (inset) an SEM image of the 60-MXene-NiCo$_2$S$_4$@NF sample after 3000 cycles.*
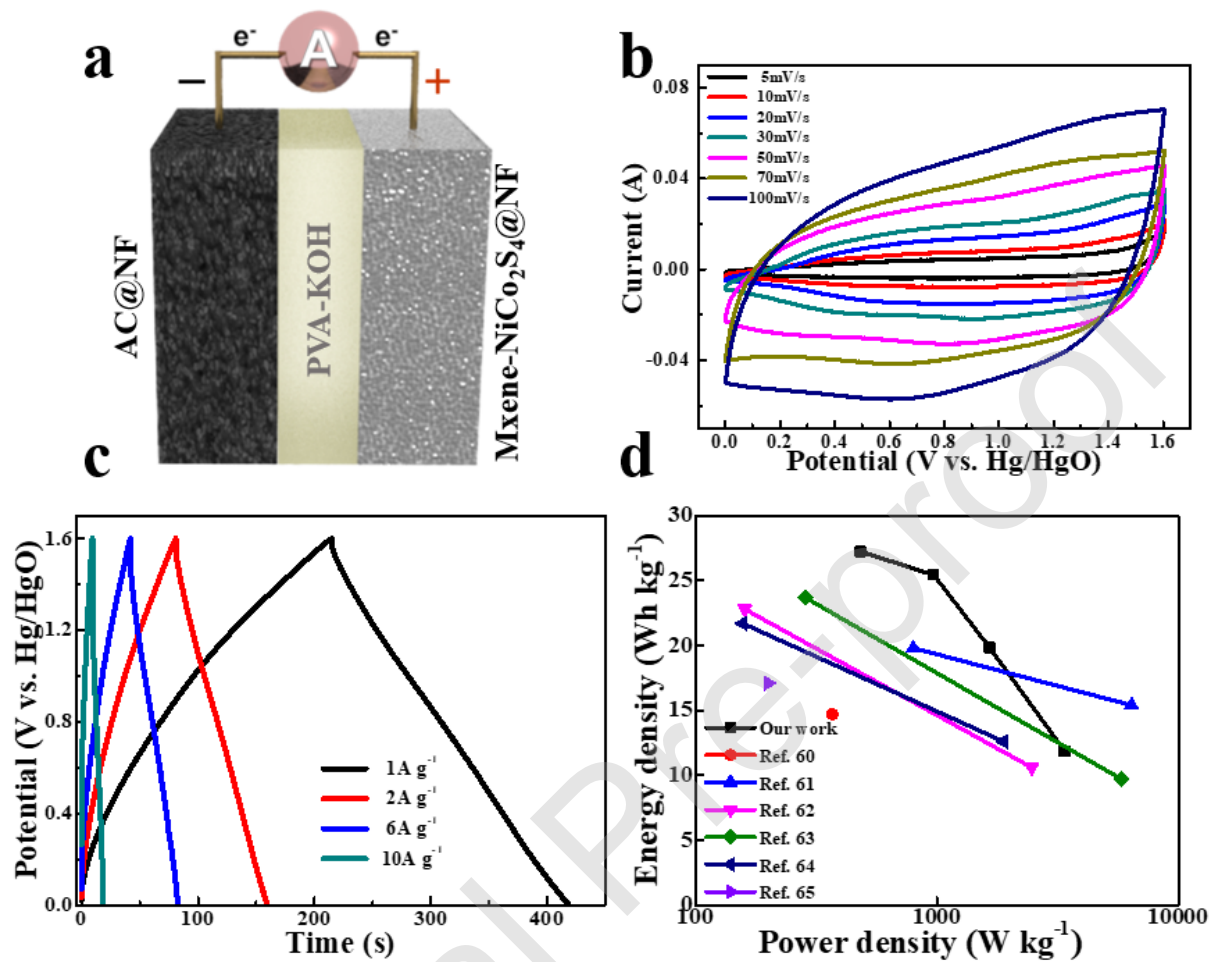
Figure 5. (a) Schematic of the ASC device; (b) CV curves of the device at various scan rates;

(c) charge-discharge curves of the device at various current densities; (d) Ragone plot of the

power density and energy of the ASC device.

Supporting Information

3D Hierarchical Transition-Metal Sulfides Deposited on MXene as Binder-Free Electrode for High-Performance Supercapacitors

Hui Li[1,&], Xin Chen[2,&], Erfan Zalezhad[3,*], K. N. Hui[4,*], K. S. Hui[5,*] and Min Jae Ko[1,*]

[1]Department of Chemical Engineering, Hanyang University, 222 Wangsimni-ro, Seongdong-gu, Seoul, 04763, Republic of Korea

2Department of Mechanical Convergence Engineering, Hanyang University, 222 Wangsimni-ro, Seongdong-gu, Seoul, 04763, Republic of Korea

3Biomechacin LLC, San Antonio, TX 78251, USA

4Institute of Applied Physics and Materials Engineering University of Macau, Avenida da Universidade, Taipa, Macau 999078, China

5School of Mathematics, University of East Anglia, Norwich NR4 7TJ, UK

*Corresponding authors
E-mail: mjko@hanyang.ac.kr (M. J. Ko); e.zalnezhad@gmail.com (E. Zalnezhad); bizhui@umac.mo (K. N. Hui); k.hui@uea.ac.uk (K. S. Hui)

& These authors equally contributed to this work.

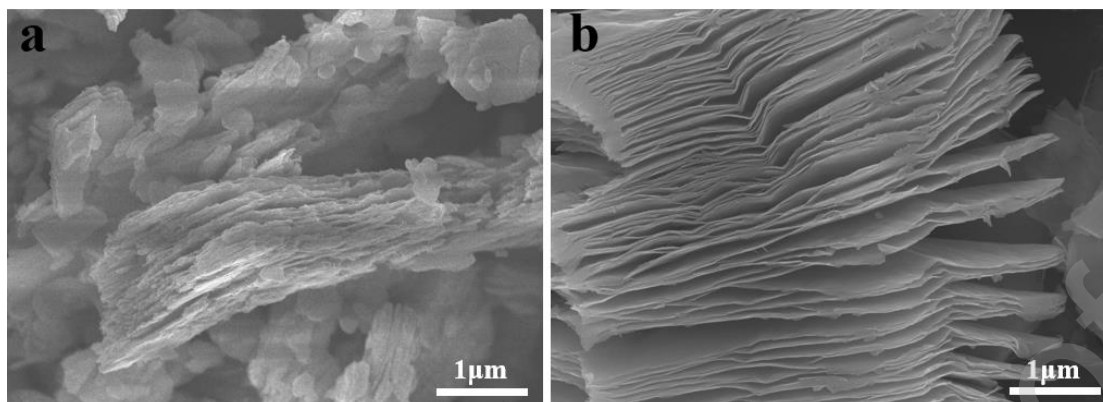Figure S1. XPS core-level spectra of the (a) Ti 2p and (b) C 1s regions.

Figure S2. Low-magnification SEM images of pure MXene powder (a) before and (b) after treatment with DMSO.
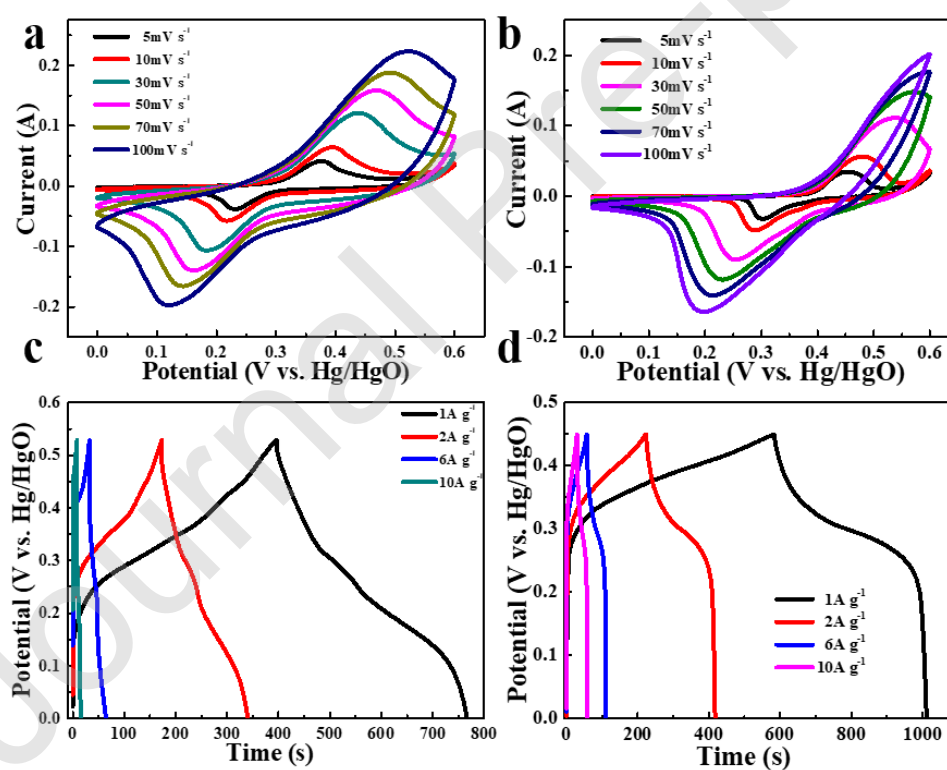

Figure S3. (a) CV and (b) GCD curves of 50-MXenes-NiCo$_2$S$_4$@NF and 70-MXenes-NiCo$_2$S$_4$@NF electrodes at different scan rates and current densities.
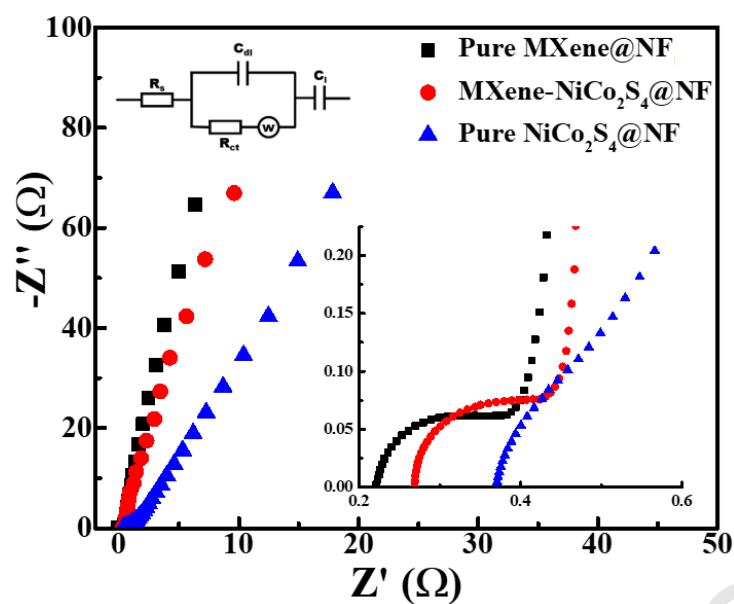
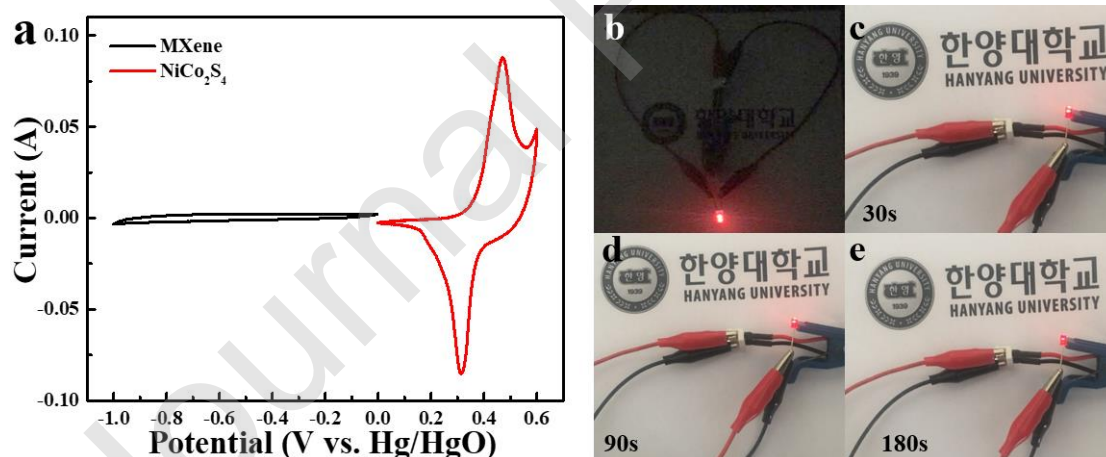*Figure S4: Nyquist plot of different samples (insets: corresponding equivalent circuit and magnified plot).*

Figure S5 (a) CV curves of the AC and MXene-NiCo$_2$S$_4$ electrodes in the three-electrode system, obtained at a scan rate of 5 mV s^{-1}; (b, c, d, e) photographs of the full cell powering an LED.

31

Table S1: EIS results for different samples

	R_0 (Ω)	C_{dl} (μF/cm^2)	R_{ct} (Ω)	W (S•sec^.5/cm^2)
Pure MXene@NF	0.21	14.18	0.88	0.0278
60-MXene-NiCo$_2$S$_4$@NF	0.26	414.9	0.92	0.037
Pure NiCo$_2$S$_4$@NF	0.37	527.16	2.77	0.0762